

INFRARED-SENSOR MODELING AND GPU SIMULATION OF TERMINAL GUIDANCE FOR ASTEROID INTERCEPT MISSIONS

Joshua Lyzhoft*, John Basart[†], and Bong Wie[‡]

This paper describes the IR-sensor modeling and simulation problem of a terminal guidance system for asteroid intercept missions. Precision terminal guidance problem of targeting small asteroids (50 to 100 meters in diameter) is investigated in this paper. Signal-to-noise ratio estimation for visual- and IR-sensors, estimation of their minimum and maximum ranges for target detection, and GPU-accelerated simulation of the IR-based terminal guidance are discussed. Scaled polyhedron models of known objects, such as the Rosetta mission's Comet 67P/C-G, OSIRIS-REx's Bennu, and asteroid 433 Eros, are utilized in developing a GPU-based simulation tool for the IR-based terminal guidance. A parallelized ray tracing algorithm for simulating realistic surface-to-surface shadowing of a given celestial body is developed. Polyhedron solid-angle approximation is also discussed.

INTRODUCTION

The Asteroid Deflection Research Center (ADRC) at Iowa State University has been developing a Hypervelocity Asteroid Intercept Vehicle (HAIV) concept to mitigate the impact threat of hazardous asteroids with short warning time [1–3]. An illustration of the proposed HAIV terminal intercept scenario is provided in Figure 1. To demonstrate the feasibility of such a mission, a scaled polyhedron model of 433 Eros was used in [4] for a closed-loop optical navigation and guidance simulation study of the HAIV concept.

When on-board visual optical tracking of an asteroid target becomes unavailable, an IR telescope/sensor might be required for precision terminal guidance. It can be seen in Figure 2 that size, with slight contribution from albedo, will affect the asteroid's signature in the IR regime, whereas for visual electromagnetic waves asteroid size and albedo play a key role in object detection and observation.

An IR sensor array has been employed for the Exoatmospheric Kill Vehicle (EKV). The EKV system is designed to intercept ballistic missiles at hypervelocity speeds [5]. The on-board focal plane array used for EKV targeting consists of a 256 by 256 structure with pixel pitch of 30 μm , which is sensitive to long wave (7 to 12 μm) and very long wave (12 to 30 μm) IR emission [6]. During the EKV targeting process, the EKV also receives information from the long wave IR sensor of the Space Based Infrared System (SBIRS) in low Earth orbit. By using this sensor, but with its unknown optics, the detection range of the system is said to be about 1000e6 kilometers for an object emitting 6e8 W/Ster. However, exact details on the signal-to-noise ratio (SNR) value for object detection and mission success for both the EKV and SBIRS are unknown [7].

*Graduate Research Assistant, Asteroid Deflection Research Center, Department of Aerospace Engineering.

[†]Professor Emeritus, Dept. of Electrical and Computer Engineering, 351 Durham Center.

[‡]Vance Coffman Endowed Chair Professor, Asteroid Deflection Research Center, Department of Aerospace Engineering,

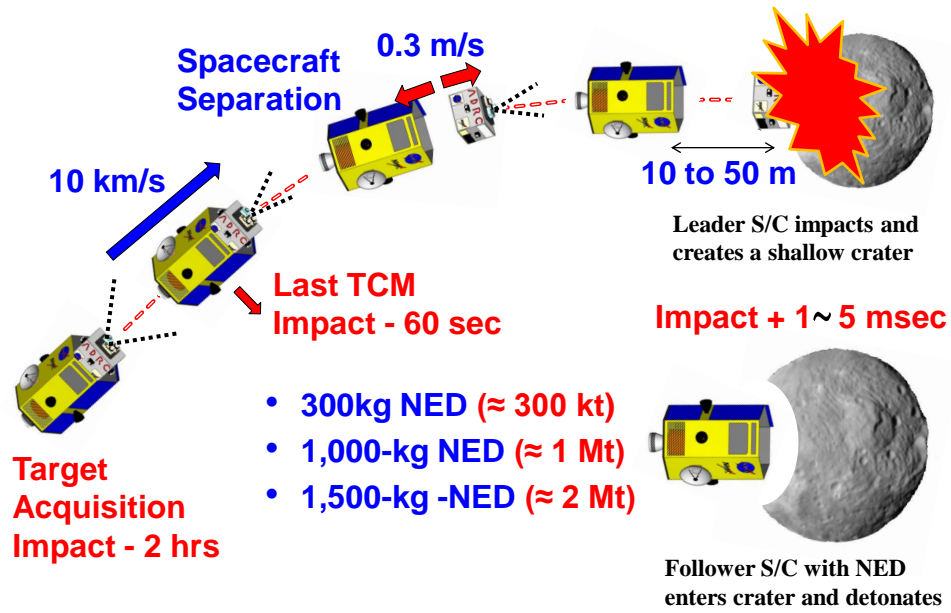


Figure 1. A baseline terminal intercept scenario of a two-body HAIV carrying a nuclear explosive device (NED).

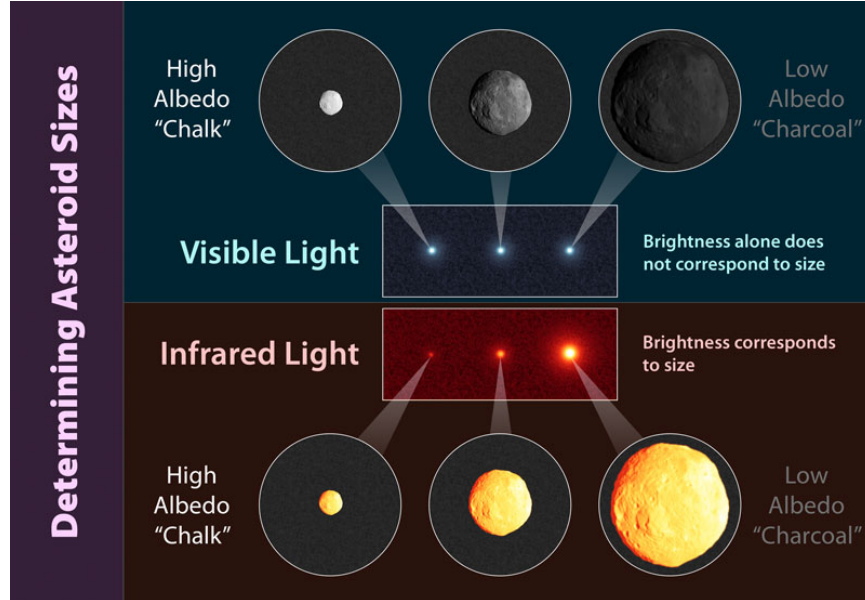


Figure 2. Comparisons of optical and infrared images of asteroids with different sizes and albedos. Image courtesy of NASA/JPL.

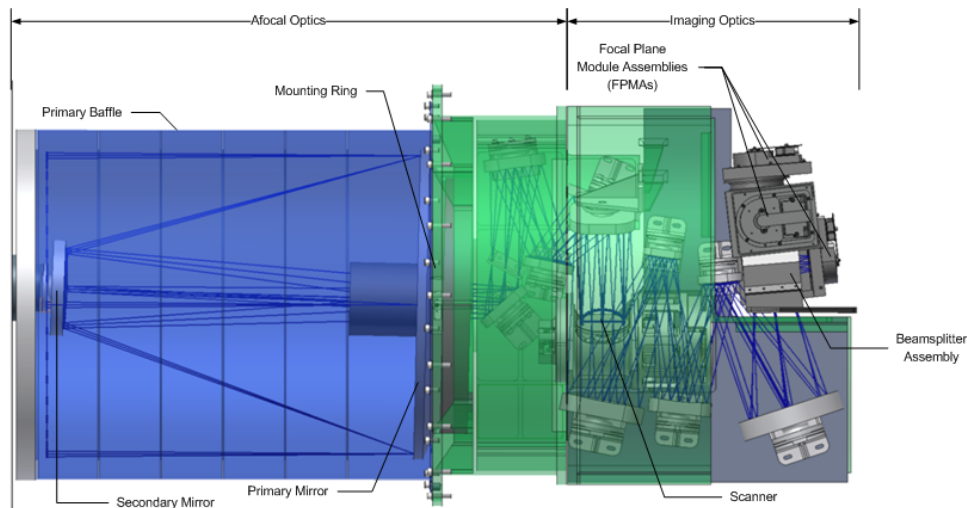


Figure 3. Illustration of the WISE IR telescope. Image courtesy of NASA/JPL.

In [8], the physical models of visual/IR sensors are characterized to estimate their SNR for a given detector and asteroid scenario in the N-band of IR wavelength. This formulation did not entirely take into account the optics of the instrument and uses a different definition for the SNR from what is presented in this paper. A reference IR telescope of the Wide-field Infrared Survey Explorer (WISE) uses a Cassegrain-like primary mirror to collect signal from objects of interest. A WISE telescope illustration can be seen in Figure 3 [9].

This paper will describe the sensor modeling and simulation problem of an IR-based terminal guidance system for asteroid intercept missions. GPU-accelerated simulation results for an IR-based terminal guidance system will be presented.

OPTICS AND VISUAL/IR SENSORS

Three types of sensors, along with their optical configurations, are studied for possible implementation to the HAIV system. The instruments of interest herein are a visual sensor, an IR sensor, and a radar. Although a radar is often excluded for hypervelocity intercept mission applications due to its inherent range/power issues, it is included in our study because of its probable need under certain circumstances. Proper parameters of these sensors are determined by estimating the SNR, which corresponds to a minimum or maximum detection distance, and characteristics of the optics to be implemented.

Classical Cassegrain Telescope

A classical Cassegrain telescope design is considered due to its simplicity and similarity to the NEOWISE infrared telescope design. The Cassegrain telescope illustrated in Figure 4 will be the basis of our study in this paper. Given an effective focal length, a primary-mirror focal length and diameter, and a back focus distance, specific telescope parameters are then determined. It can be seen that baffling and glare stops discussed in [10] were not taken into account in our study.

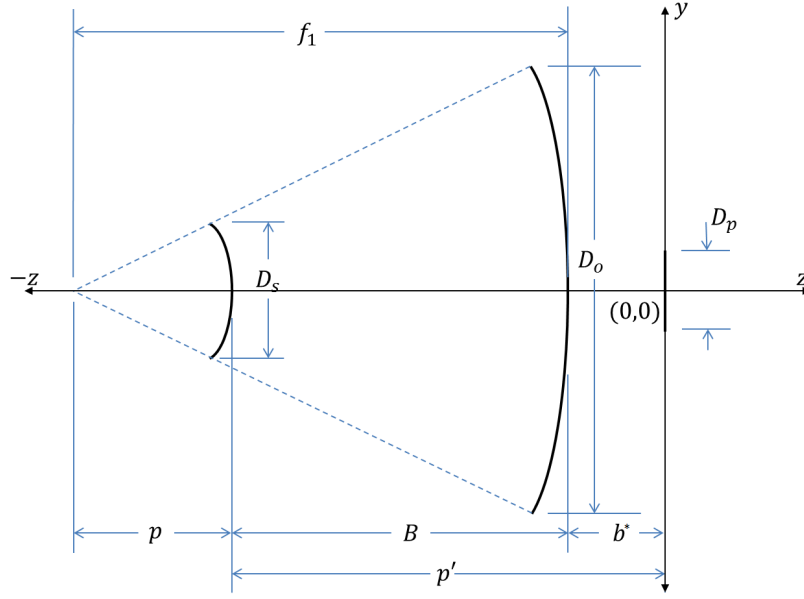


Figure 4. Design parameters of a classical Cassegrain telescope.

The magnification of the system is

$$M = \frac{F}{f_1} \quad (1)$$

where F and f_1 are the system focal length and the primary mirror focal length. Once magnification is calculated, other parameters of this system are found. Given the back focus (distance from the primary mirror to the focal plane), b^* , the primary mirror focus intercept point is found as

$$p = \frac{F + b^*}{M + 1} \quad (2)$$

The overall distance from the secondary mirror to the focal plane, also known as the secondary to Cassegrain focus p' , is given by

$$p' = pM \quad (3)$$

From the Cassegrain focus, the mirror separation, B , is found as

$$B = p' - b^* \quad (4)$$

Another very important part of the Cassegrain telescope is to design the size of the secondary mirror. This diameter, D_s , can be found as

$$D_s = \frac{pD_o}{f_1} + \frac{BD_p}{f_1 M} \quad (5)$$

where D_p is the minimum diameter of the image plane (not including thickness). This correlates to the size of the imaging device, which is equivalent to the minimum dimension of the array.

The radius of curvature (ROC) is found for both, the primary mirror and secondary mirror and is given by

$$R_1 = 2f_1 \quad (6)$$

and

$$R_2 = \frac{2}{\frac{1}{p} - \frac{1}{p'}} \quad (7)$$

where R_1 is the ROC for the primary mirror and R_2 is the ROC for the secondary mirror. By using the ROC of each mirror, the prescription for the two mirrors can be found by the formulas

$$z_1 = \frac{y_1^2}{2R_1} - b^* \quad (8)$$

$$z_2 = \frac{y_2^2/R_2}{1 + \sqrt{1 - (1 + b_2)(y_2/R_2)^2}} - (b^* + B) \quad (9)$$

and

$$b_2 = \frac{-4M}{(M - 1)^2} - 1 \quad (10)$$

where z_1 and z_2 are face locations of the mirrors when the image plane array is located at the origin of a measurement, $\frac{-D_o}{2} \leq y_1 \leq \frac{-D_o}{2}$, and $\frac{-D_s}{2} \leq y_2 \leq \frac{-D_s}{2}$. This is only valid in the case of a Classical Cassegrain telescope.

When looking through a telescope, the magnification, the primary mirror diameter, and the image plane size (array size or eye pupil diameter) compound to vary the brightness of the image. The brightness coefficient takes into account the light grasp and magnification of the device to give the maximum amount of light that is illuminating the device as

$$a_{opt} = \left(\frac{D_o}{10 M D_p} \right)^2 \quad (11)$$

A way to interpret this coefficient is to use the same telescope but different eye pieces to enlarge the image size at the entrance of the eye pupil. This spreads the same amount of light out onto a larger area, hence creating a dimmer object. There is a similar form used in finding irradiance at a detector, which is given in [11].

Visual- and IR-Sensors

The imaging characteristics of visual- and IR-sensors discussed in this section. The first steps of estimating the SNR is to integrate Planck's law for black body radiation over the visual band of electromagnetic spectrum, which gives the radiance. Figure 5 illustrates the black body curves for the IR regime of interest for the electromagnetic spectrum. An assumption is made where IR and visual waves are not transmitted through the body and only reflected energy and emitted energy are considered.

The radiance ($\text{W m}^{-2} \text{sr}^{-1}$) and irradiance (W m^{-2}) for reflected energy are formulated as follows. Radiance is given by

$$L_{Vs_i} = \int_{\lambda_1}^{\lambda_2} \frac{2hc^2}{\lambda^5} \frac{1}{e^{\frac{hc}{k_B T_{sun\lambda}}} - 1} d\lambda \quad (12)$$

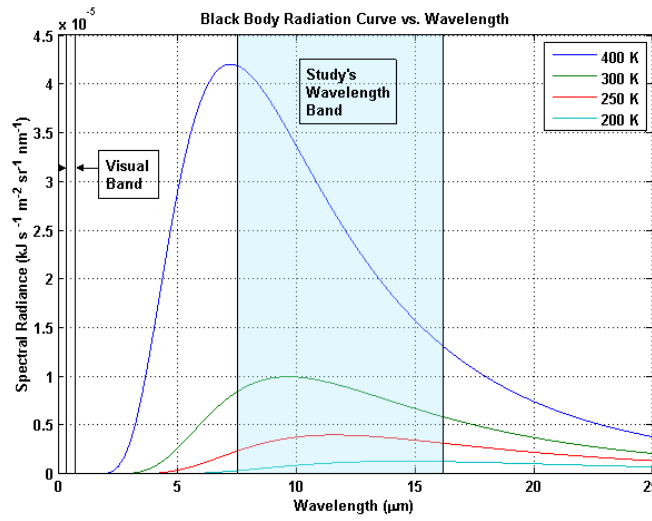


Figure 5. Black body radiation for different temperature values in the IR regime.

where the temperature of interest is that of the sun, h is the Planck's constant ($6.6260695710^{-34} \text{ m}^2 \text{ kg s}^{-1}$), c is the speed of light, k_B is the Boltzmann constant ($1.380648810^{-23} \text{ m}^2 \text{ kg s}^{-2} \text{ K}^{-1}$), λ_1 is the lower bound wavelength, and λ_2 is the upper bound wavelength. Since this is calculated, one must evaluate the radiance of the sun at the body, which is the irradiance multiplied by the sun's solid angle. An assumption is made that the sun's solid angle can use a circular approximation, since the asteroid's distance from the sun is much larger than the radius of the sun.

This leads to the incident irradiance at the object as

$$E_{V_{s_i}} = L_{V_{s_i}} \frac{\pi r_s^2}{d_{s/obj}^2} \quad (13)$$

where r_s is the radius of the sun and $d_{s/obj}$ is the distance from the sun to the object. The irradiance of the reflected electromagnetic waves, from the object as seen by the spacecraft, is given by

$$E_{V_{reflected}} = \alpha_V E_{V_{s_i}} \Omega_{reflected} \quad (14)$$

where α_V is the asteroid's visual albedo, r_{obj} is the radius of the object, $\Omega_{reflected}$ is the solid angle for reflected irradiance, and $d_{obj/sc}$ is the distance from the object to the spacecraft. Here it is also assumed that the solid angle of the object can be given by a circular approximation due to its radius being much smaller than the distance from the asteroid to the spacecraft. The variable, β , corresponds to the number of illuminated polyhedron faces seen by the spacecraft compared to the total number of faces illuminated by the sun. This variable will be discussed more in-depth later. Since the reflected energy's irradiance is estimated, the emitted energy from the object must be calculated.

The emitted energy from the body is very similar to reflected energy obtained by an integration of Planck's law using the temperature of the object, as follows:

$$L_{V_{emitted}} = \epsilon_V \int_{\lambda_1}^{\lambda_2} \frac{2hc^2}{\lambda^5} \frac{1}{e^{\frac{hc}{k_B T_{obj} \lambda}} - 1} d\lambda \quad (15)$$

where ϵ_V is the object's visual emissivity. This assumes that there is no transitivity, which is the case for the infrared band as well. Once again, the irradiance can be found by multiplying the radiance by the solid angle (circular approximation), as follows:

$$E_{V_{emitted}} = L_{V_{emitted}} \Omega_{emitted} \quad (16)$$

where $\Omega_{emitted}$ is the solid angle for emitted irradiance. The total irradiance seen by the spacecraft is then given by

$$E_V = E_{V_{reflected}} + E_{V_{emitted}} \quad (17)$$

In general, the irradiance at the spacecraft from the visual emission can be neglected, therefore $E_{V_{emitted}} \approx 0$, and E_V is reduced to $E_V = E_{V_{reflected}}$. From the irradiance, the photon flux, given in number of photons per square meter per second, is calculated as follows:

$$\Phi_V = \frac{E_V \lambda_{max}}{hc} \quad (18)$$

where λ_{max} is the wavelength of peak emission, which is a function of Wien's displacement constant and the Sun's temperature.

By collecting the device parameters and the photon flux at the device, the signal given on the CCD array in number of electrons is obtained as

$$H_{V_{signal}} = a_{opt} \Phi_V \tau_{opt} \eta G_V \tau_{int} N \pi \left(\frac{D_o}{2} \right)^2 \quad (19)$$

where a_{opt} is a coefficient from the optics, τ_{opt} is the optics' efficiency, η is the device's quantum efficiency, G_V is the device's photoconductive gain, τ_{int} is the device's integration time, N is the number of image samples, and D_o is the diameter of the primary mirror or lens. A similar expression can be found in [12].

Equation (19) is also used in IR signal formulation, which has IR specific variables. For the SNR to be calculated, the estimated standard deviations of the noise must be found. The noise characteristics of the device are dictated by the following expressions:

$$\sigma_{V_{shot}} = \sqrt{H_{V_{signal}}} \quad (20)$$

$$\sigma_{V_{dark}} = \sqrt{\tilde{n}_V n_{pix} N \tau_{int}} \quad (21)$$

where the standard deviations are in number of photons and follow Poisson statistics, \tilde{n}_V is the number of electrons per second per pixel, and n_{pix} is the total number of pixels. Equations (20) and (21) can be found in [13], but in similar forms. These equations will also be applied to the IR sensor. Since these noise values are assumed to be statistically independent, the total noise standard deviation is described as

$$\sigma_{V_{noise}} = \sqrt{\sigma_{V_{shot}}^2 + \sigma_{V_{dark}}^2 + R_r^2} \quad (22)$$

where R_r is the read-in noise. This value is usually given as an RMS value measured in number of electrons. The final expression for the SNR in the visual band becomes

$$SNR_V = \frac{H_{V_{signal}}}{\sigma_{V_{noise}}} \quad (23)$$

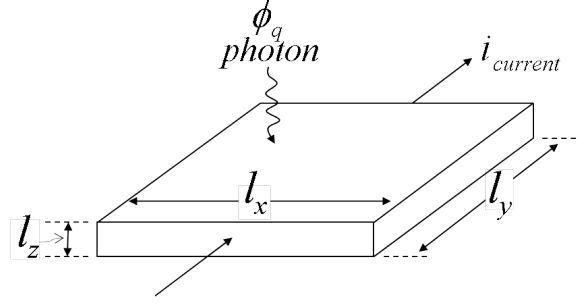


Figure 6. A simple illustration of sensor pixel characteristics.

Similar to the visual sensor, the IR sensor is characterized by also using Planck's law of black body radiation. Again, this equation is integrated over the infrared wavelengths, which calculates the radiance of the object. However, the emissivity is taken into account.

In Figure 5, black body radiation curves for different asteroid temperatures are shown, and the band in a transparent blue represents the infrared wavelengths of this study. The radiance and irradiance for emitted and reflected are given as

$$L_{IR_{emitted}} = \epsilon_{IR} \int_{\lambda_1}^{\lambda_2} \frac{2hc^2}{\lambda^5} \frac{1}{e^{\frac{hc}{k_B T_{obj} \lambda}} - 1} d\lambda \quad (24)$$

$$E_{IR_{emitted}} = L_{IR_{emitted}} \Omega_{emitted} \quad (25)$$

$$L_{IR_{s_i}} = \int_{\lambda_1}^{\lambda_2} \frac{2hc^2}{\lambda^5} \frac{1}{e^{\frac{hc}{k_B T_{sun} \lambda}} - 1} d\lambda \quad (26)$$

$$E_{IR_{reflected}} = \alpha_{IR} L_{IR_{s_i}} \Omega_{reflected} \frac{\pi r_s^2}{d_{s/obj}^2} \quad (27)$$

$$E_{IR} = E_{IR_{emitted}} + E_{IR_{reflected}} \quad (28)$$

where ϵ_{IR} is the IR emissivity of the object, α_{IR} is the object's IR albedo, λ_1 and λ_2 are the IR lower and upper bound wavelengths. Note that these equations must be integrated over the infrared spectrum regime of interest. To find the radiance for reflected energy and emitted energy, they are not integrated over the visual spectrum like in the visual camera section, but over infrared wavelengths.

Following similar steps from that of the visual camera, the photon flux and signal are described as follows:

$$\Phi_{IR} = \frac{E_{IR} \lambda_{max}}{hc} \quad (29)$$

$$H_{IR_{signal}} = a_{opt} \Phi_{IR} \tau_{opt} \eta G_{IR} \tau_{int} N \pi \left(\frac{D_{mirror}}{2} \right)^2 \quad (30)$$

where the λ_{max} is the wavelength of peak emission, which is a function of Wien's displacement constant and object's temperature and G_{IR} is the IR device gain. With signal photons known, noise characteristics need to be developed.

Four types of noise sources are considered herein: shot noise, dark current noise, Johnson noise, and generation-recombination noise. The standard deviations of each noise can be described as

$$\sigma_{IR_{shot}} = \sqrt{H_{IR_{signal}}} \quad (31)$$

$$\sigma_{IR_{dark}} = \sqrt{\tilde{n}_{IR} n_{pix} N \tau_{int}} \quad (32)$$

$$\sigma_{IR_{johnson}} = \sqrt{\frac{2k_B T_d l_x l_z N \tau_{int}}{\rho l_y q^2}} \quad (33)$$

$$\sigma_{IR_{GR}} = G \sqrt{2\eta \Phi_{IR} \tau_{opt} A_d N \tau_{int}} \quad (34)$$

where \tilde{n}_{IR} is the number of electrons per second per pixel, T_d is the detectors' temperature, (l_x, l_y, l_z) are pixel dimensions, ρ is the resistivity, q is charge of an electron, and A_d is the area of the detector.

Similar forms of Equations (31) through (34) can be found in [13, 14]. An illustration of a simple sensor pixel can be seen in Figure 6. If the noises are assumed to be statistically independent of each other, then the total noise standard deviation for the infrared regime is given by

$$\sigma_{IR} = \sqrt{\sigma_{IR_{shot}}^2 + \sigma_{IR_{dark}}^2 + \sigma_{IR_{johnson}}^2 + \sigma_{IR_{GR}}^2} \quad (35)$$

From the formulated IR signal and noise equations, the SNR in the infrared band of interest takes the same form as that of the visual band, which is the ratio of estimated signal to the calculated noise standard deviation, given by

$$SNR_{IR} = \frac{H_{IR_{signal}}}{\sigma_{IR}} \quad (36)$$

Image Rendering and Solid-Angle Approximation

The visual camera is simulated by incorporating the albedo of a given target and assigning values to polyhedron shape model faces according to the direction of the sun vector with the asteroid. This sun vector, \hat{S} , is the unit vector pointing from the sun to the target [15]. Each polyhedron face coefficient is described as

$$C_i = \begin{cases} k_d (\hat{N}_i \cdot -\hat{S}) + k_a & \text{if } (\hat{N}_i \cdot -\hat{S}) > 0 \\ 0 & \text{if } (\hat{N}_i \cdot -\hat{S}) \leq 0 \end{cases} \quad (37)$$

where i is the face index, \hat{N}_i is the outward pointing unit normal vector of each face, k_d is the diffuse lighting coefficient associated with the object's albedo, and k_a is the ambient lighting coefficient. By using this vector, including a ray trace algorithm for shadowing, and exploiting the advantages of parallel computing, realistic images can be generated quickly. Such images can be seen in Figures 7 and 8. These images, however, are computed in greyscale.

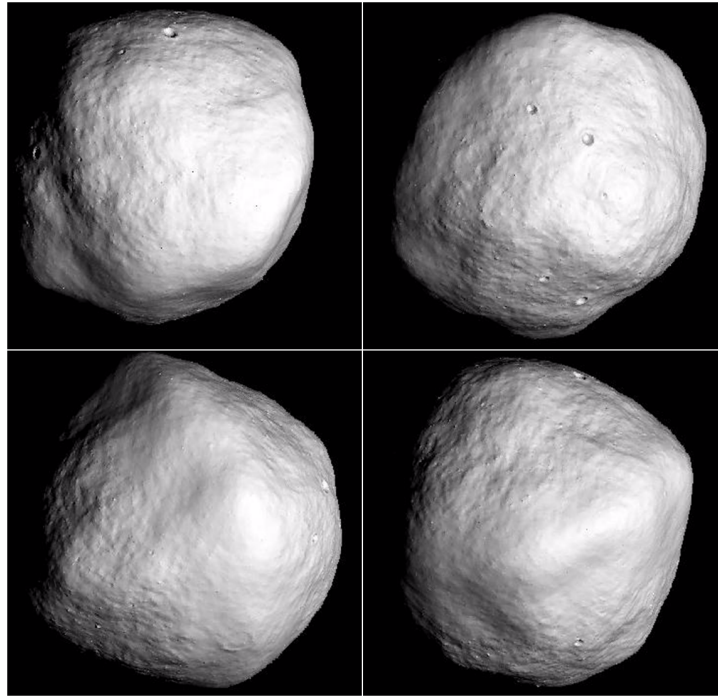


Figure 7. Computer-generated Bennu polyhedron model with shadowing.

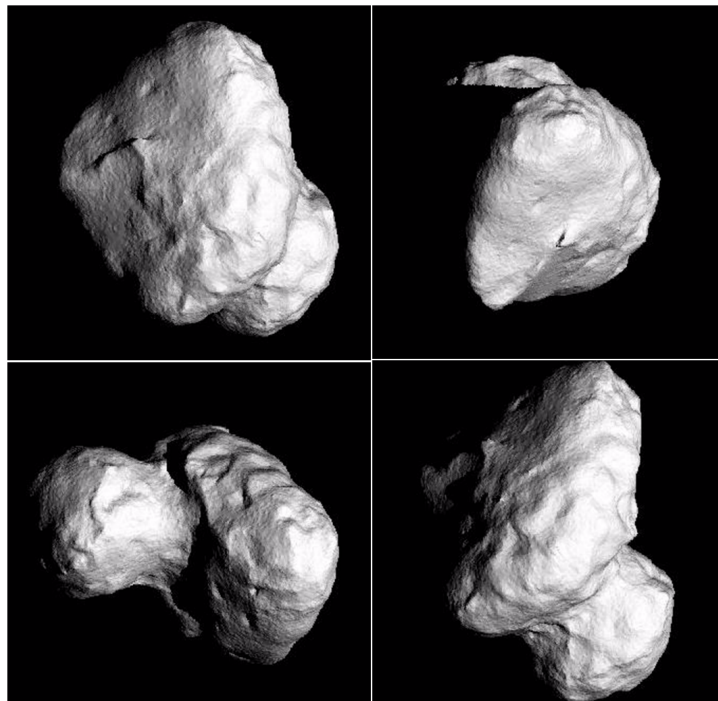


Figure 8. Computer-generated 67P/Churyumov-Gerasimenko polyhedron model with shadowing.

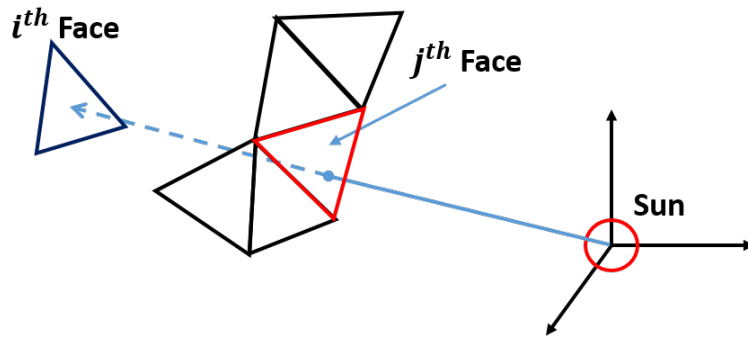


Figure 9. Depiction of j^{th} face intersecting a vector to the i^{th} face.

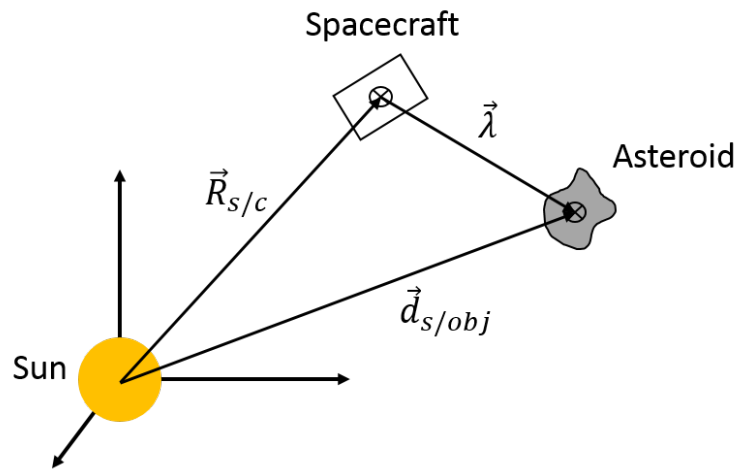


Figure 10. Depiction of asteroid and asteroid position vectors along with the line-of-sight vector.

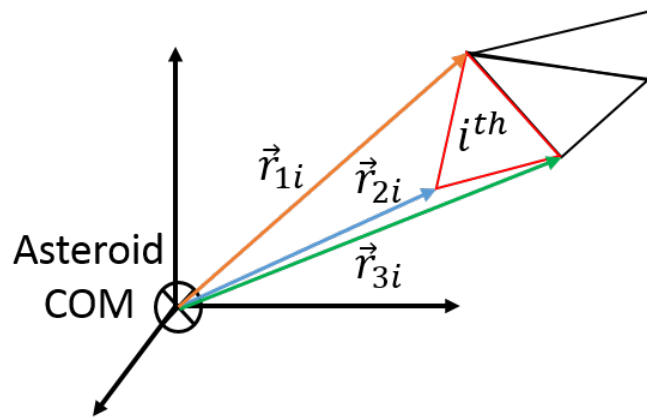


Figure 11. The face and vertex vectors of asteroid polyhedron model. Coordinates of each face are relative to the center-of-mass of the object.

These computer generated images are depictions of Bennu and Comet 67P/C-G, which are taken at different times within a simulation where the respective body is rotating about a reference axis. As can be seen in these figures, there is crater shadowing. The shadowing is obtained by a GPU-accelerated ray tracing algorithm. By applying this algorithm, the face coefficient for any given face i becomes zero under the following condition: there exists a face j that intersects the vector from the sun to the i th face, where the intersecting j th face is located between the sun and the i th face. An illustration of the face intersection can be seen in Figure 9. This shadowing effect will help simulating landing on a target or tracking rendezvous locations.

After the coefficients for the visible faces of the polyhedron are calculated, the solid angle for an extended object can be found. This can be done by projecting the visible triangular faces onto a plane that is perpendicular to the line of sight vector and summing the areas of these projected faces. Figure 10 depicts the line of sight vector, and Figure 11 shows the vectors associated with the i^{th} face vertex. The equations for the projected i^{th} face's vertex vectors are given by

$$\vec{R}_{1i} = \vec{r}_{1i} - \left(\vec{r}_{1i} \cdot \frac{\vec{\lambda}}{|\vec{\lambda}|} \right) \frac{\vec{\lambda}}{|\vec{\lambda}|} \quad (38)$$

$$\vec{R}_{2i} = \vec{r}_{2i} - \left(\vec{r}_{2i} \cdot \frac{\vec{\lambda}}{|\vec{\lambda}|} \right) \frac{\vec{\lambda}}{|\vec{\lambda}|} \quad (39)$$

$$\vec{R}_{3i} = \vec{r}_{3i} - \left(\vec{r}_{3i} \cdot \frac{\vec{\lambda}}{|\vec{\lambda}|} \right) \frac{\vec{\lambda}}{|\vec{\lambda}|} \quad (40)$$

where \vec{r}_{1i} , \vec{r}_{2i} , and \vec{r}_{3i} are the i^{th} face's vertices, $\vec{\lambda}$ is the line-of-sight from the spacecraft to the asteroid, and \vec{R}_{1i} through \vec{R}_{3i} are the projected faces. With the projected vertices found, the areas of each triangular face can be calculated. Each i^{th} faces' area is given by

$$S_i = \frac{|\left(\vec{R}_{3i} - \vec{R}_{1i} \right) \times \left(\vec{R}_{3i} - \vec{R}_{2i} \right)|}{2} \quad (41)$$

where S_i is the area of the i^{th} face corresponding to its projected triangle. The sum of all the visible triangles' area becomes the solid angle as

$$\Omega = \frac{\sum_{i=1}^n S_i}{|\vec{\lambda}|^2} \quad (42)$$

where Ω is the object's solid angle and n is the total number of visible faces. This is done for both the emitted and reflected portions of the irradiance, which would give $\Omega_{emitted}$ and $\Omega_{reflected}$. Note that this approximation only holds when the radius of the object is much smaller than the distance between itself and the spacecraft, $|\vec{\lambda}|$.

Reflected irradiance solid angle is calculated on the GPU by calculated finding the surface area of each triangle that can be seen by both the sun and the spacecraft. These are the intersection faces of both the views. Emitted irradiance solid angle is calculated in a similar manner. However, the triangular areas needed are only from those viewed by the spacecraft. The process for finding the solid angle approximation is done at each time step.

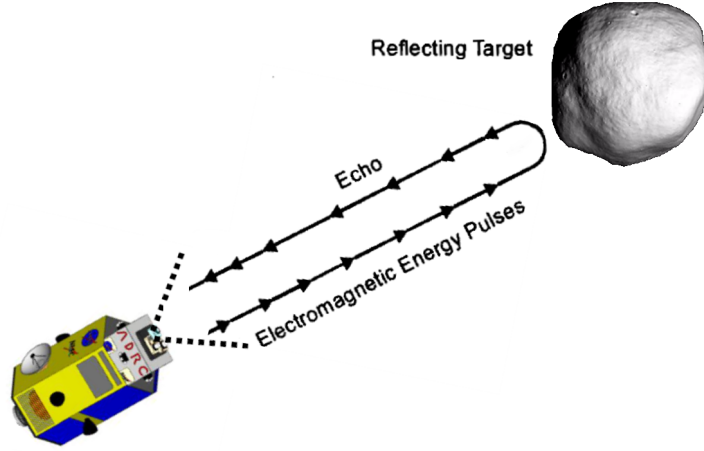


Figure 12. Illustration of a mono-static radar system (not to scale).

Radars

Object range determination for a mono-static system (transmitter and receiver are collocated) is found. An illustration of a mono-static system is depicted in Figure 12. The radar expression is manipulated to find the maximum detection distance. A minimum detection distance is also required since there is a transition from the near-field to the far-field of the signal. The transition distance from the near-field to the far-field is given in [16]. There is still signal received in the near-field, but may give incorrect values. These two equations are given by

$$R_{max} = \sqrt[4]{\frac{P_t K_{losses} G^2 \lambda^2 \sigma N^{1/2}}{(4\pi)^3 k_B T_e \Delta f (SNR)_R}} \quad (43)$$

$$R_{min} = \frac{2D^2}{\lambda} \quad (44)$$

where P_t is the peak pulse power transmitted, K_{loss} are the loss of the device, G is the antenna gain, λ is the radar wavelength, σ is the object's radar cross section, N is the number of samples, T_e is the equivalent noise temperature, Δf is the bandwidth, $(SNR)_R$ is the desired signal-to-noise ratio, and D is the primary signal-collecting dish's diameter (assuming a circular dish). Variables of other devices should not be confused with radar parameters.

COMPARISON OF SENSORS AND SIMULATION RESULTS

Comparison of Sensors

Comparison of the sensing devices discussed in the preceding sections is provided herein. This entails the asteroid's detection distance, which corresponds to device's SNR, and image representation given SNR values. These images are plotted using a Matlab program and the calculated standard deviation of the noise.

Table 1. Visual-sensor design results and asteroid parameters

Instrument Characteristics	Value	Asteroid Parameters	Value
F	8 m	T_{ast}	300 K
M	8	r_{ast}	25 m
D_o	0.4 m	$d_{s/obj}$	1.496e8 km
b^*	0.08 m	$d_{obj/sc}$	4.18e4 km
η	0.7	α	0.25
G_V	6.83		
τ_{optics}	0.504		
N	1		
τ_{int}	8.8 sec		
\tilde{n}_V	5 e/pix/sec		
n_{pix}	$1024 \times 1024 = 1,048,576$ pixels		
N_r	1 e/pix/sec		
Pixel Pitch	18 μ m		
λ_1, λ_2	380, 800 nm		

Various parameter values of the visual and IR detection devices are kept very similar to those of the NEOWISE telescope. They include the temperature for IR sensor array at approximately 7.8 Kelvin. By using the formulation for the signal-to-noise ratio and the values given in Tables 1 and 2, the results for the SNR value of approximately 10 are provided in Tables 3 and 4. Results illustrate the geometric pixel fill corresponding to the largest dimension of the object, as well as the visual magnitude. These tables show that the geometric pixel fill of the object is less than one, which means there is no object detail resolved but detected. The visual magnitude is calculated from the flux density of the object in both IR and visual wavelengths. In both cases, the reference celestial object is Vega, with an assumed visual magnitude of 0.03 (N band and visual band).

As can be noticed, the distance from the object to the spacecraft is different, between the visual and IR sensor, by almost a factor of 34.8. This means that the IR device can detect a 50-meter object, with N band emissivity of 0.9, about 34 times than the visual device. Moreover, in the visual band, the albedo of the asteroid is set at 0.25, which is a high value for an asteroid. With these parameters, the detection distances and selected asteroid sizes can be seen in Figure 13. In these plots, the lines for detection distance are linear due to the assumption of the solid angle being subtended by a circular approximation, along with other approximations using polyhedron face plane projections.

As stated previously, parameters of the radar device are different from the other two sensing devices. By using the equations describing the radar, an estimation of minimum and maximum

Table 2. IR-sensor design results and asteroid parameters

Instrument Characteristics	Value	Asteroid Parameters	Value
F	8 m	T_{ast}	300 K
M	8	r_{ast}	25 m
D_o	0.4 m	$d_{s/obj}$	1.496e8 km
b^*	0.08 m	$d_{obj/sc}$	1.45e6 km
η	0.7	ϵ	0.9
G_{IR}	6.83		
τ_{optics}	0.504		
N	1		
τ_{int}	8.8 sec		
\tilde{n}_{IR}	5 e/pix/sec		
n_{pix}	$1024 \times 1024 = 1048576$ pixels		
R_d	5.0e04 Ω		
Pixel Pitch	18 μm		
λ_1, λ_2	7.5, 16.5 μm		

Table 3. Asteroid detection results for a visual sensor

Parameters	Value
Geometric Optics Pixel Fill	<1
Visual Magnitude	≈ 6.13
$(SNR)_V$	≈ 9.9

Table 4. Asteroid detection results for an IR sensor

Parameters	Value
Geometric Optics Pixel Fill	<1
Visual Magnitude (N band)	≈ 5.9
$(SNR)_{IR}$	≈ 10

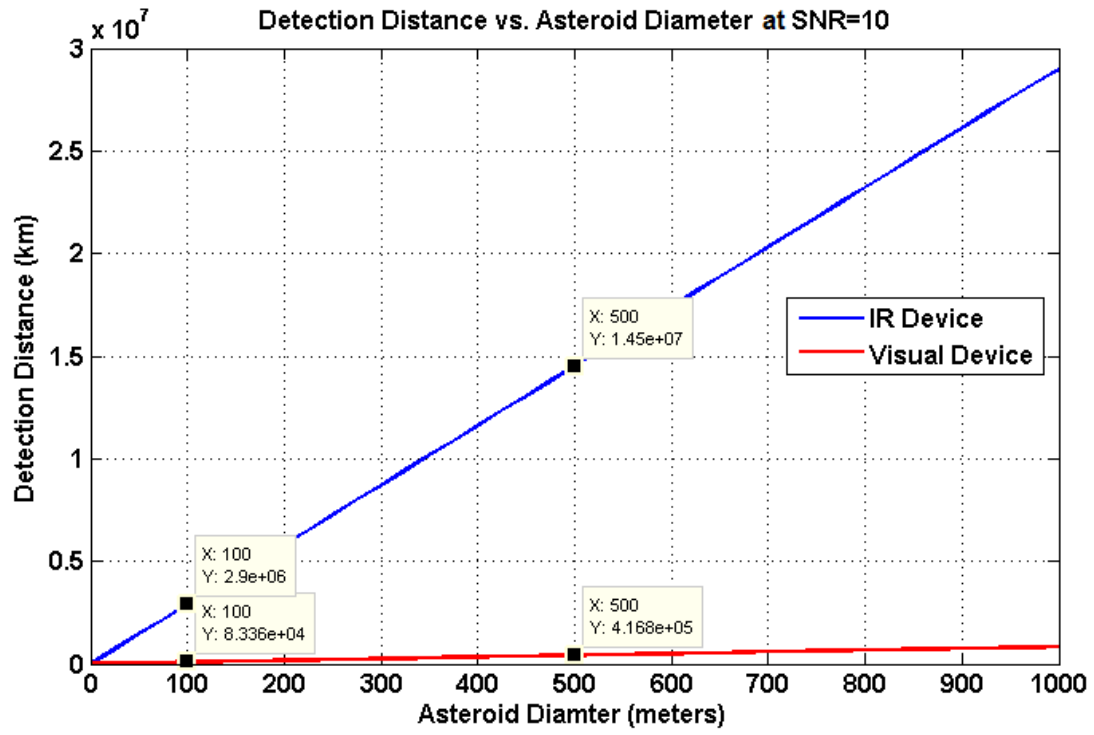


Figure 13. Detection distances vs. asteroid diameter for IR and visual band sensors.

Table 5. A reference radar design

Instrument Characteristics	Value
P_t	500 W
K_{loss}	0.55
scale	1/10
G	8.0568e5
λ (scaled)	3.5 mm
σ (scaled)	340 m ²
N	1000
t_s (Pulse Width)	1 μ s
T_e	70 K
Δf (1/ t_s)	1.0e6 Hz
$(SNR)_R$	10
D	1 m

Table 6. Comparison of IR- and visual-sensors for terminal guidance (optical components are the same as in previous comparison)

Simulation Results	IR	Visual
$d_{obj/sc}$ at 2 hours	7.2e4 km	7.2e4 km
Visual Magnitude at 2 hours	-0.654	7.312
Geom. Pixel Fill at 2 hours	<1	<1
SNR at 2 hours	4.055e3	3.351
$d_{obj/sc}$ at 60 seconds	600 km	600 km
Visual Magnitude at 60 seconds	-11.10	-3.134
Geom. Pixel Fill at 60 seconds	≈ 37	≈ 37
SNR at 60 seconds	3.125e7	4.813e4

detection distances can be found. A scaled Bennu model is used here to evaluate the radar performance. Bennu is scaled by 1/10, resulting in a diameter around 50 meters. When scaling Bennu, the transmitted signal's wavelength must also be scaled by the same factor, if similar detection distances are desired. At a wavelength of 3.5 cm, a unscaled Bennu has a radar cross-section of $3.4e4 \text{ m}^2$, which correlates to a scaled σ_r of 340 meters and a wavelength of 3.5 mm. This creates a needed wavelength that is near the edge of the radar regime of the electromagnetic spectrum but is still obtainable.

By using the values in Table 5, the radar equations result in a maximum detection distance of 9.062e2 km. However, the minimum distance is dictated by the far-field and near-field transition, if there are no filtering techniques applied. This minimum distance before near-field transition measures 571 meters. Rendezvousing with a target body and landing on its surface would need a radar device that has a lower minimum detection range.

Terminal Guidance Simulation Results

Hypervelocity intercept missions are simulated using a scaled 433 Eros polyhedron model. The points of interest are at two hours and 60 seconds before impact. Figure 14 compares the visual and infrared sensors at 60 seconds before asteroid intercept. These simulated images were obtained by using the parameters given in Tables 1 and 2, along with Cassegrain telescope design. It can be seen

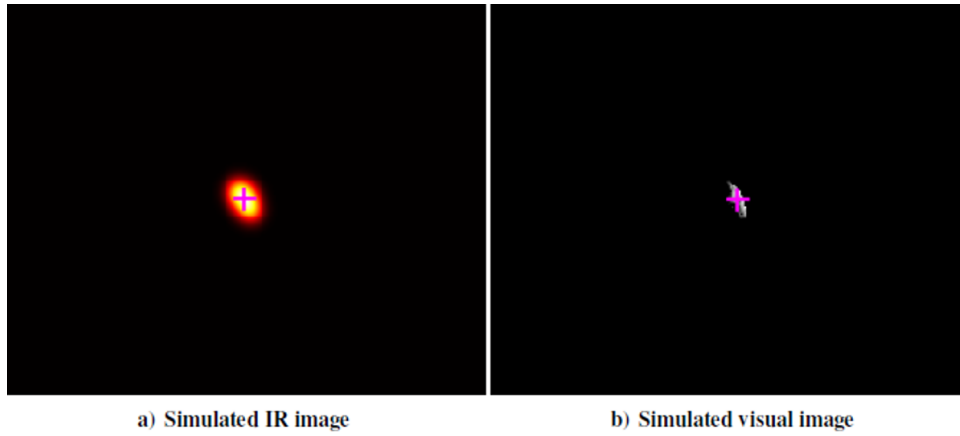


Figure 14. Examples of IR and visual sensor images at 60 seconds prior to final impact.

that the asteroid does not fill many pixels on the sensor array. The calculated amount of pixels filled for the maximum dimension of the asteroid can be seen in Table 6. This table also includes the SNR for both times of interest. Two hours before impact, each sensor array displays sub-pixel pixel fill. However, at 60 seconds before impact, the horizontal pixel fill is at approximately 37 pixels. In both the sensor scenarios, 2 hours or 60 seconds before impact, the pixel fill does not provide detailed target images.

It can be seen that the SNRs at two hours before impact are quite different for both devices. At this point, the IR device can discern the asteroid, whereas the visual device does not have an adequate SNR. This shows for lower albedo asteroids, which are small and have higher emissivity, that the IR device may out-perform the visual device. Consequently, the guidance algorithms use the information from the IR device and radar. Radar is used once the distance from the asteroid to the spacecraft is sufficient enough for radar detection, which was stated to be about 900 km.

For the guidance simulations, a hybrid algorithm is used. This includes kinematic intercept guidance, which uses predetermined control pulses and proportional navigation. During the beginning of the terminal phase of the mission, the spacecraft undergoes kinematic impulse guidance, and once a sufficient amount of pixels is filled on the sensor array by the target, the guidance algorithm is switched to proportional navigation guidance to ensure mission success. A depiction of the control accelerations can be seen in Figure 15.

Using this same control acceleration, at 60 seconds before impact, the spacecraft will separate into a fore and aft body system [17]. At this separation time, a position and velocity error are placed on the fore and aft bodies. This simulation is conducted 3,000 times. After these simulations, approximately 98.5 percent of the fore bodies and 98.7 percent of the aft bodies impact in the IR case. In comparison, only 93.4 percent impacted of both fore and aft bodies for the visual case. A depiction of these simulations are shown in Figure 16. This figure, green dots represent the fore body, while red dots represent the aft body.

CONCLUSION

In this paper, the sensor modeling and simulation problem of an IR-based terminal guidance system for asteroid intercept missions has been discussed. In particular, the formulas for signal-

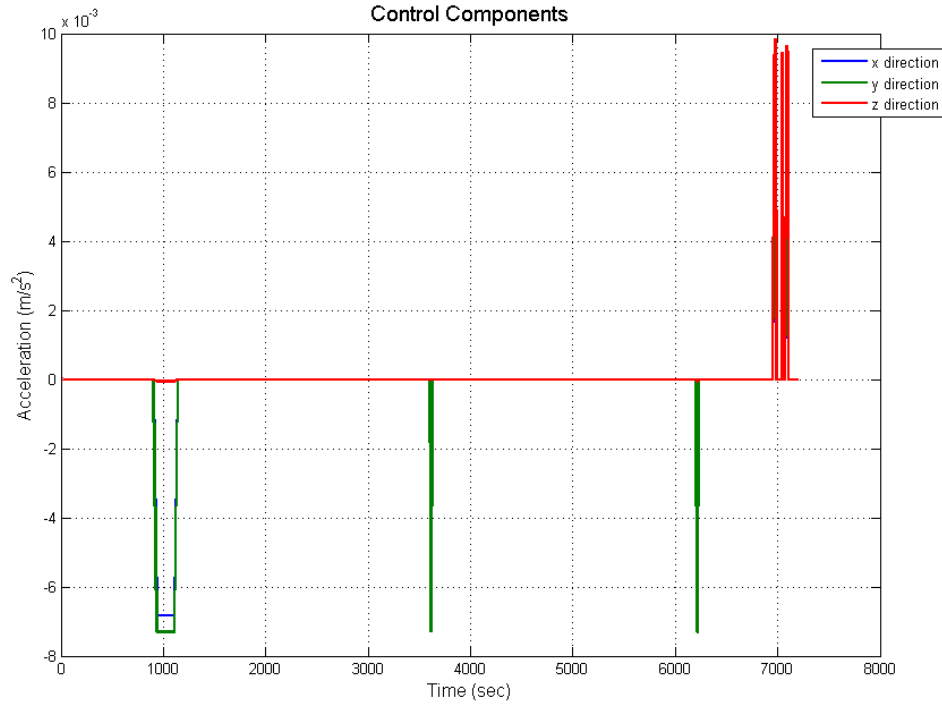


Figure 15. Control acceleration time history of an IR-based terminal guidance system (t=0 implies 2 hours before impact).

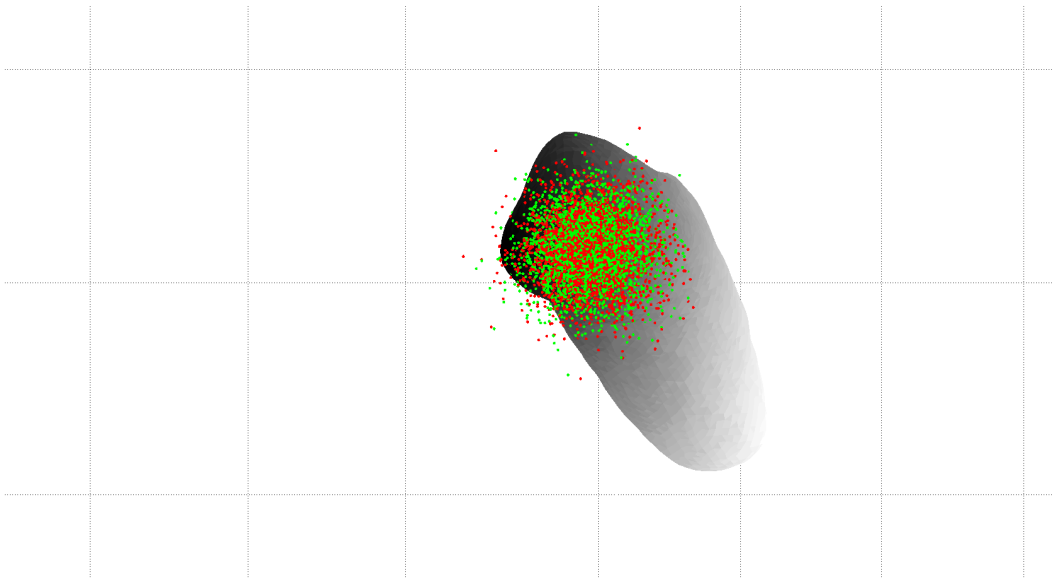


Figure 16. Monte Carlo simulation result for intercepting a 50-meter asteroid using an IR-based terminal guidance system for a reference HAIV mission.

to-noise ratio estimation and detection distance estimation for visual- and IR-sensors have been derived. In addition, estimation of the solid angle of an object due to shadowing was studied, which relates to object irradiance. By following the procedures described in this paper, maximum detection distances were found for various sensing devices. These distances, corresponding to a 50-meter asteroid, were estimated to be 4.18e4 km for a visual sensor, 1.46e6 km for an IR sensor, and 906.2 km for a radar. These results show that for an asteroid with an IR emissivity of 0.9 and a visual albedo of 0.25, the IR sensor detects the asteroid at a distance 34 times farther than the visual sensing device.

REFERENCES

- [1] Wie, B. "Hypervelocity Nuclear Interceptors for Asteroid Disruption," *Acta Astronautica*, 90, 2013, pp. 146-155.
- [2] Pitz, A., Kaplinger, B., Vardaxis, G., Winkler, T., and Wie, B., "Conceptual Design of a Hypervelocity Asteroid Intercept Vehicle (HAIV) and Its Flight Validation Mission," *Acta Astronautica*, 94, 2014, pp. 42-56.
- [3] Barbee, B., Wie, B., Steiner, M., and Getzandanner, K., "Conceptual Design of a Flight Demonstration Mission for Hypervelocity Asteroid Intercept Vehicle (HAIV)," *Acta Astronautica*, 106, 2015, pp. 139-159.
- [4] Lyzhoft, J., Hawkins, M., Kaplinger, B., and Wie, B., "GPU-Based Optical Navigation and Terminal Guidance Simulation of a Hypervelocity Asteroid Impact Vehicle (HAIV)," AIAA-2013-4966, it AIAA Guidance, Navigation, and Control Conference, Boston, MA, August 19-22, 2013.
- [5] Wie, B. et al., *An Innovative Solution to NASA's NEO Impact Threat Mitigation Grand Challenge and Flight Validation Mission Architecture Development*, Final Report for NIAC Phase 2 Study, December 9, 2014. http://www.nasa.gov/sites/default/files/files/Bong_Wi_Final_Report.pdf
- [6] Herring, J. et al., *Staring 256 X 256 LWIR Focal Plane Array Performance of the Raytheon Exoatmospheric Kill Vehicle*, 1998. www.dtic.mil/cgi-bin/GetTRDoc?AD=ADA400061
- [7] Sessler, A. M. et al., *Countermeasures: A Technical Evaluation of the Operational Effectiveness of the Planned US National Missile Defense System*, MIT Security Studies Program, Union of Concerned Scientists, April 2000.
- [8] Lyzhoft, J., Groath, D., and Wie, B., "Optical and Infrared Sensor Fusion for Hypervelocity Asteroid Intercept Guidance," AAS 14-421, *AAS/AIAA Space Flight Mechanics Meeting*, Santa Fe, NM, January 26-30, 2014.
- [9] "WISE Preliminary Release Explanatory Supplement: WISE Flight System and Operations." *WISE Preliminary Release Explanatory Supplement*. N.p., 12 April 2011. Web. 7 April 2014. http://wise2.ipac.caltech.edu/docs/release/prelim/expsup/sec3_2.html.
- [10] Lyzhoft, J. and Wie, B., "IR Telescope and Sensor Characterization for Hypervelocity Asteroid Intercept Guidance," AIAA-2014-4299, *AIAA/AAS Astrodynamics Specialist Conference*, San Diego, CA, August 4-7, 2014.
- [11] Schowengerdt, R., "RADIOMETRY OF LAMBERTIAN SOURCES," Class Notes, ECE 425 Image Science and Engineering, The University of Arizona, Tucson, Arizona. Spring Semester 2000.
- [12] Rieke, J. H., *Detection of Light: from the Ultraviolet to the Submillimeter*, 1st ed., Cambridge University Press, New York, 1994, pp. 56.
- [13] Bolte, M., "Signal-to-Noise in Optical Astronomy." Class Lecture, Modern Observational Techniques, University of California, Santa Cruz.
- [14] Dereniak, E. L., Boreman, G. D., *Infrared Detectors and Systems*, John Wiley & Sons, New York, 1996, Ch. 5.
- [15] Kaplinger, B., "Physical modeling and high-performance GPU computing for characterization interception, and disruption of hazardous near-Earth objects," Ph.D. Thesis, Iowa State University, 2013
- [16] Fenn, A. J., "Near-Field Testing of Adaptive Radar Systems," *The Lincoln Laboratory Journal*, Vol. 3, No. 1, 1990, pp. 23-40.
- [17] Zimmerman, B. and Wie, B., "GPU-Accelerated Computational Tool Development for Studying the Effectiveness of Nuclear Subsurface Explosions, IAA-PDC-15-03-15, IAA Planetary Defense Conference, Roma, Italy, April 2015.